# EFFICIENT AND ROBUST ALGORITHMS FOR THE REAL-TIME OPTICAL TRACKING OF SPACE DEBRIS

**Julian Rodriguez-Villamizar and Thomas Schildknecht**

*Astronomical Institute University of Bern (AIUB), Sidlerstrasse 5, 3012 Bern , Switzerland, Email: julian.rodriguez@aiub.unibe.ch*

## ABSTRACT

The latest European Space Agency Annual Space Environment Report [4] confirms, once more, the ever increasing amount of space debris orbiting around the Earth. Collisions between resident space objects will only accelerate the growth rate of the current debris population endangering space-related activities. In that context, the surveillance of the outer space becomes of paramount relevance. Current existing surveillance networks make extensive use of different observation techniques to retrieve not only updated information of the orbital elements of the object, but also evidence about its attitude and attitude motion.
One on-going limitation for the tracking of space debris with optical sensors (active or passive) comes from the lack of accurate ephemerides that will not allow pinpointing the object within the field of view of the sensor. The constraint imposed by the field of view is significantly less stringent in passive-optical systems, but becomes critical for active systems such as laser ranging stations.
The presented work focuses on the development of algorithms that allow an automated real-time correction of the pointing of the telescope while the object is within the field of view of the wide angle camera. The final aim is the centring of the target within the narrow field of view of the laser beam, thus facilitating the acquisition of laser ranges. We choose estimators according to statistical properties such as efficiency and robustness to enable the tracking even in the most challenging observation conditions: daytime. All experiments were conducted using real data derived from a tracking camera with a scientific-CMOS sensor on the Zimmerwald Laser and Astrometry Telescope (ZIMLAT) at the Swiss Optical Ground Station and Geodynamics Observatory Zimmerwald (SwissOGS) operated by the Astronomical Institute of the University of Bern, Switzerland.

Keywords: Satellite Laser Raning, Object Recognition, Active Tracking.

## 1. INTRODUCTION

The last revision of the Space Debris Mitigation Guidelines issued by The Inter-Agency Space Debris Coordination Committee (IADC) [6] supports the sustainable use of the outer space through:

- Limiting the probability of accidental collision in orbit.
- Limiting the long-term presence of spacecraft and launch vehicle orbital stages in the low-Earth orbit (LEO) region after the end of their mission.

The previous two guidelines, out of the total of 7, highlight the importance of a surveillance and tracking global network. Note that the second mitigation guideline asks for surveillance to ensure that the disposal of decommissioned satellites and launch vehicle orbital stages are compliant with the original proposal and will not pose a future risk for space-related activities.
The ground-based monitoring of the outer space is usually conducted by sky surveys and specific target's follow-up observation schemes. Nonetheless, when the reduction of uncertainty in the target state becomes imperative due to a close conjunction, or due to the occurrence of a re-entry event, a combination of the prior observing techniques raises: the stare and chase. This observation strategy could be implemented either using prior information of the target, or for first discoveries fixing the telescope in a given direction, e.g. in the zenith.
The one pass real-time observation of targets with poor ephemerides presents a challenge: we want to maximize the portion of the observed arc and maximize the likelihood to retrieve range and angular measurements. In previous studies [8], we showed that the use of merged observations, distributed along the maximal observable orbital arc, will facilitate the re-acquisition of targets for the same station and to other stations by disseminating the new ephemerides through the propagation of the newly estimated state. Through this work we will present the core algorithms used by the stare and chase. Specifically, we will derive efficient and robust estimates for the object recognition and the tracking modules. The combination of the two modules define our active tracking approach

where the system starts the tracking using existing orbital information from the target. Next, once images are acquired, and the target object is successfully identified in the camera reference frame, differential corrections are estimated and the pointing of the telescope is rectified with respect to the initial pointing derived from the given orbit.

## 2. EFFICIENT AND ROBUST ESTIMATORS

Through our work, we will use robust and efficient estimators. The metric defined for the robustness is the breakdown point [9], while for the efficiency we choose estimators that yield minimum dispersion estimates [9]. An example of a robust estimator is the sample median; likewise, an example of an efficient estimator is the sample mean. Next, we will list situations where the selection of a suitable estimator is of paramount relevance:

- To mitigate the impact of different error sources in the estimation of source and background in the passive system. Potential error sources could be due to hot and dead pixels in the imaging sensor, stray light from the laser beam, if used in combination with an active system, presence of clouds or star trails within the field of view of the sensor.
- During the object recognition phase during daylight, the terminator or nighttime if close to a celestial or artificial bright object. The brightness of the background might be close to the one of the source challenging the localization of the object image in the frame.
- During the active tracking, for deriving best estimates of the pointing of the telescope in real time. Note that inaccurate and unreliable estimates coming only from the object recognition module could lead in worse-case scenarios to hardware failures, e.g. wrong slew movements of the telescope.

For the fulfilment of the previous points, a combination of robust and efficient estimators is selected as the preferred choice for estimating the properties of the object image, i.e. the centroid and brightness, as well as its future position in the camera reference frame using the historical records available from successful detections. Finally, once we are able to track the object for the complete pass, we update its state and propagate it for next acquisitions.

## 3. IMAGE PROCESSING

In this section we will analyse all steps concerning the object recognition phase and the estimation of the so-called centroid, i.e. the coordinates of the object image on the camera reference system, which describe the central tendency for the location of the distribution of its intensity on the image plane. The input for the image processing module are images acquired in real time. The output will be estimates of the centroid coordinates for the object image. The latter will be the input for the tracking algorithm. Moreover, we will show that the implementation of our algorithm allow us to derive the apparent brightness of the target as a by-product of the object recognition phase.

### 3.1. Problem statement

Given a raw image and the orientation of the camera reference system with respect to a defined reference system of interest, e.g. the horizon reference system, find the coordinates of the object image so that, after applying the transformation between camera and horizon reference systems, angular observations, i.e. azimuth an elevation, can be derived.
To tackle the problem we divide the acquired image into two classes: source and background. The source corresponds to those solar photons scattered by the target, which reach the detector. The background comprises sky background photons, detector dark current, dead and hot pixels, etc. In general, the background represents all input signal which triggered an event on the detector despite not coming from the source. Due to the aforementioned variability of the background attributed to the different error sources, we apply a sequence of steps to smooth and remove the background and improve the estimation of the centroid.

### 3.2. Pre-Processing

In this step we apply a lowpass filter in order to enhance the quality of the object image by filtering potential imaging errors, which will affect otherwise the estimation of the background and the source. We refer to imaging errors as sample pixels that provide intensity values not drawn from the expected probability distribution of either the background or the source. The selected choice for the filter is the *robust* median kernel. The operation consists on placing a matrix of a defined size in each of the image pixels, and computing the median of all elements within it; the resulting value will overwrite the old value for the pixel where the matrix was placed. This pre-processing step was implemented as a discrete convolution in the spatial domain, meaning that we include another tuning parameter besides the kernel size, the step size, which will allow to improve the computational performance of the operation. In Subsection 3.5 we will show the impact of selecting different tuning parameters.

### 3.3. Background Estimation and Removal

An image taken by our tracking camera contains 5.5 megapixels. The object image will be represented in only a fraction of the total number of pixels. In order to reduce the size of the image we crop the original raw image into a smaller one. To answer the question: where do you crop your image without also removing the object of interest? we implemented two different options. First, we use the estimated position of the laser beam on the camera reference system (further details are given e.g. in [3]) and crop the raw image according to a predefined width considering an average apparent velocity of a low Earth orbiter for crossing the diagonal field of view of the tracking camera, which is of about 9 arcminutes. That works when we have accurate ephemerides, e.g. those generated for active targets of the International Laser Ranging Service (ILRS) [7] in the form of Consolidated Predicted Format (CPF). In the space debris domain usually the ephemerides are computed from the so-called Two Line Elements (TLE) [1], which can have significant offsets with respect to the true position of the object in the sky. In the latter case, the operator must select where the object is during the first frame acquired by the tracking camera and only afterwards the image is cropped. Note that this approach was implemented only for cases where the signal-to-noise ratio was compromised, e.g. during daylight, and the automated operating mode will remove the target after the pre-processing step preventing the immediate tracking of the target.

Once we have the subframe, and initial coordinates of the centroid, we can compute the intensity as a function of the distance between all pixels within the subframe and the centroid. By doing so, we are approximating the point spread function (PSF) of the object image. Note that the PSF will represent mainly the on-site atmospheric seeing, i.e. we use the mathematical function describing the seeing-induced PSF as a first-order approximation of the PSF of the object image. To derive the radius of the source on the image, we compute it using the full-width-at-half-maximum (FWHM) calculated numerically using the previously constructed radial distribution of intensity with respect to the centroid. The radii for the inner and outer background apertures are the result of the product between the FWHM and a defined constant (more details are available in [2]). In our case we took twice the value taken in [2] to consider potential errors in the estimation of the centroid.

The difference between outer and inner background radii defines a region within the subframe that might be used as a representative sample of the background. For the approximation of the PSF, we use circular apertures assuming a symmetrical PSF, which might be found in ideal imaging systems observing with long exposure, averaging the impact of the on-site atmospheric seeing. From the computational point of view, the calculation of circular apertures involve the computation of the distance between all pixels within the subframe and the centroid of the object image. The previous operation can be avoided if we take the circumscribed square of the outer minus the one of the inner aperture.

In Figure 1 we show the subframe of the image, and the area that will be used to extract the samples for the estimation of the background using circular and square apertures. The raw image has a radiometric resolution of 16 bit and, as it can be seen in the raw subframe, the used dynamic range is that of 18% of its total capacity. The example shows a nighttime frame acquired for Topex-Poseidon using an exposure time of 0.05 seconds. Additionally, from visual inspection, we see that the extracted background using squares is more heterogeneous, in this case, than the one using circles, in particular the lower right and left corners. It is clear that the geometrical pattern is not the cause, but rather the fact that the square apertures reach a brighter region of the background that is more heterogeneous for this specific frame.

In Table 1 we compare the estimation of the background for each case evinced in Figure 1. Our ground truth is defined by the values estimated using the circular apertures. The reason is that we computed the normality Kolmogorov-Smirnov statistical test, and it succeeded at a confidence level of 95% using the samples contained in the background ring. Despite the fact that the background is more heterogeneous when using squares, the estimates for the background using the sample mean and median are close to the ones provided by our ground truth. The difference can be neglected if one considers the dynamical range of the image. The estimated background using the complete subframe, including the source, show the expected increase in the magnitude for the background estimated using the sample mean, but the impact of the source is significantly attenuated when using the sample median. Note that despite including the source within the estimation of the background, due to the large number of samples, the impact of the source is further attenuated. Regarding the estimators measuring the dispersion, we see no difference between the estimation of the variance with respect to the mean or median due to the large number of samples for each of the 3 cases. The latter result is commonly found in actual symmetric distributions. The estimated standard deviation with respect to the sample mean and sample median reflects the heterogeneity of the background containing the source when estimating the background using the subframe. Finally, when taking the median absolute deviation, a robust estimator to measure the dispersion of a set of samples, we see that it is able to isolate those pixels that do not belong to the homogeneous distribution of the background, i.e. the source.

We conclude that the use of robust estimators for the reckoning of the background, as well as for its dispersion, mitigates the impact of error sources not coming from its expected distribution. We proved the previous statement computing the background including the source itself, which may be considered an extreme case. We implemented the described approach in our real-time system using the square apertures besides the median and median absolute deviation as estimators for the background.

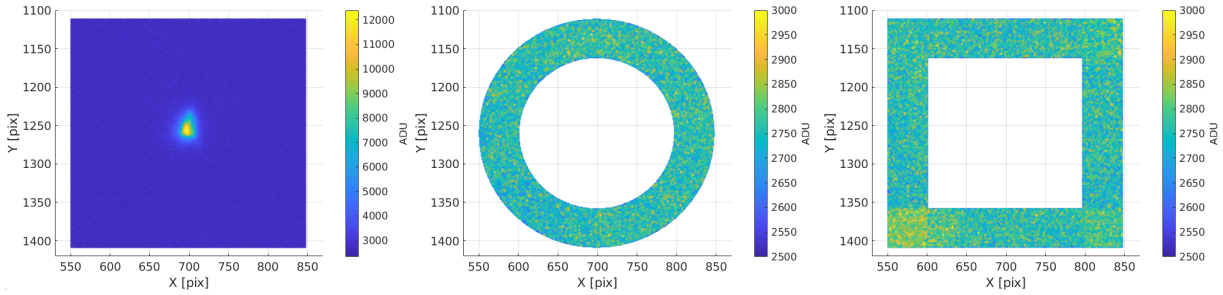


*Figure 1. Subframe of original image centered on the object image (left). Area of the subframe defined by the difference between outer and inner background radii (middle). Area of the subframe taking the circumscribed square of the difference between outer and inner background radii (right). Unit colobars: Analog-To-Digital (ADU) units.*

*Table 1. Estimation of the background varying the geometrical pattern from where samples of the background are extracted. Std: standard deviation. Mad: median absolute deviation. We highlight in gray the combination of estimators that minimize the impact of the source in the estimation of the background.*

| | Circle | Square | Subframe |
|---|---|---|---|
| Num. Samples | 38300 | 59400 | 88209 |
| Sample Mean [ADU] | 2661 | 2664 | 2715 |
| Sample Median [ADU] | 2661 | 2663 | 2672 |
| Std. Mean [ADU] | 86 | 89 | 422 |
| Std. Median [ADU] | 86 | 89 | 424 |
| Mad. Mean [ADU] | 58 | 58 | 70 |
| Mad. Median [ADU] | 58 | 58 | 58 |

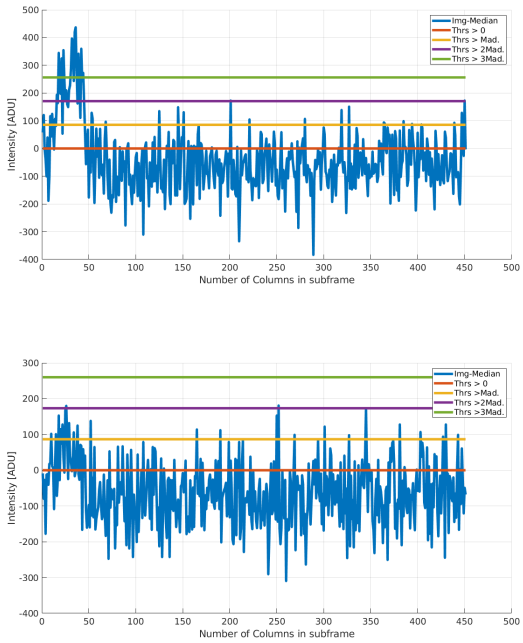


*Figure 2. Profiles of two frames acquired during the observation of a Topex-Poseidon pass using the tracking camera. The top plot shows that there is enough contrast to distinguish the object image compared to the bottom one. The figure highlights the impact of choosing a specific threshold for the removal of the background.*

Once we have representative estimates for the background, the next step is its removal. To see the impact of removing the estimated $MED(back) + kMAD(back)$, where $k$ is a constant, $MED$ the median operator, $MAD$ the median absolute deviation with respect to the median and $back$ is the set of background samples, we extracted two cross-sections from two different frames acquired from the Topex-Poseidon pass, where the object was deeply embedded in background noise. For the statistical interpretation of $k$ the reader is referred to [9]. In Figure 2 we show two profiles of the object image fixing the row. After the subtraction of only $MED(back)$, it becomes clear that a suitable threshold for masking the pixels which do not belong to the source is zero. Nevertheless, the zero threshold will not maximize the removal of the background, i.e. there will be scattered pixels which not belonging to the source will impact the determination of the centroid. The threshold $MED(back)+MAD(back)$ was found to yield a good compromise between high and low contrast images. Larger values for $k$ will work for brighter targets but may remove the weak signal of the source for images with low signal-to-noise ratio (see bottom plot in Figure 2).

Once we are able to remove the background, we proceed with the estimation of the centroid.

### 3.4. Centroid Estimation

The estimation of the centroid is given by the weighted average of the coordinates of the source pixels defining as weighting factor the intensity at the location of the different $N$ pixels within its distribution. The formula reads [5]:

$$X_{CoG} = \frac{\sum_{i=0}^{N-1} I_{x,y} X}{\sum_{i=0}^{N-1} I_{x,y}}, \tag{1}$$

where $X_{CoG}$ is the coordinate component for the center of gravity of the object image with an intensity $I_{x,y}$ at a given coordinate component $X$. Note that the estimator used for finding the centroid minimizes *the weighted mean square error*. At this stage, after the pre-processing steps decribed in Subsection 3.2, and the estimation and

removal of the background analyzed in Subsection 3.3, we minimize the contribution of background pixels in the estimation of the centroid for the source. In Subsection 3.5 we will show the results after the two operations in a sequential fashion.

### 3.5. Results and Discussion

In this Subsection we will analyze the sequence of operations performed for the extraction of the object's centroid. We present one pass for the rocket body H-2A with NORAD 38341, which has an altitude of 585 km at the perigee and culminated at an elevation of 23°on October 11, 2019, at 15:45 UTC. Note that the observation conditions, daylight and the low elevation pass, present a challenge to distinguish the source from the background. In Figure 3 we show the sequence of operations performed to discriminate the source from the background. From the left to the right we show the raw subframed image, the resulting image after the convolution between the raw subframed image and the median filter using two combinations of kernel and step size (top and bottom plots), the resulting image after subtracting $MED(back) + MAD(back)$, and finally the resulting image masking all non-positive pixels to zero.

We show one image out of the 750 acquired with an exposure time of 0.02 seconds. Note that we show how the previous centroid of the image was not optimally estimated since the background pixels were not correctly removed (upper sequence of images in Figure 3). Despite being suboptimal, the solution using a kernel of 5 pixels x 5 pixels with a step size of 3 pixels keeps the target within the subframe. On the other hand, the solution using a kernel of 9 pixels x 9 pixels with a step size of 5 pixels keeps the target centered within the subframe, after a better removal of the background in the previous image. The reason is clear: a larger combination between kernel and step size smooths better the intensity in the whole subframe. Note also that the smoothing affects the intensity of the source. After the analysis of this series, we noticed that the dynamic range yield 76% out of its full capacity for the raw subframes. The impact of the on-site atmospheric seeing becomes noticeable in many frames due to the short exposure freezing the seeing at the acquisition of the frame. Finally, we can estimate the limit of the kernel size by taking the atmospheric seeing. Example: for an atmospheric seeing of 2 arcseconds and a pixel scale of 0.173 arcseconds/pixel the limit will be a kernel size of 11 pixels x 11 pixels. A kernel size larger than the limit might remove the target from the subframe preventing the estimation of its centroid.
Finally, after the estimation of the centroid, we can estimate again the PSF, place the apertures for the source and the inner and outer apertures for the background and derive the apparent brightness of the target.

## 4. ACTIVE TRACKING

The output of the object recognition phase is the position of the object image in the camera reference system and its apparent brightness. Knowing the position of the laser beam in the camera reference system, we can estimate the offset between the target and the laser beam position. After the transformation between the camera and the horizon reference systems, those offsets are expressed as $\Delta azimuth$ and $\Delta elevation$. Despite the elaborated object recognition algorithm, nothing prevents it from failing in case of the presence of clouds, bright artificial or celestial objects within the subframe, or very low intensity contrast between source and background. For those cases, an active tracking algorithm is developed to ensure the smooth tracking of the object when the estimates derived from the object recognition phase are of compromised precision or accuracy.

### 4.1. Problem Statement

Given a set of past records of the state vector of the object image in the camera reference frame, extracted from the object recognition phase, estimate predictions at an epoch $t+1$ for the state vector of the object image, updating its state at epoch $t$ when a new observation becomes available, using the $n$ number of past records collected until the epoch $t$. The $n$ last records define our sliding observation window ($sow$).
In order to model the trajectory $T(t)$ of the object image in the camera reference frame, we make use of the Taylor series expansion:

$$T(t) = \sum_{p=0}^{p_{max}} \frac{T(t)^p}{p!}(t_0 - t)^p, \tag{2}$$

where $t_0$ is the initial entry of the sliding observation window. The predictions for the epoch $t+1$ are derived after the estimation of the $\frac{T(t)^p}{p!}$ coefficients via the minimization of *the mean square error* using all $n$ observations available within the sliding observation window. Note that the algebraic form of Equation 2 is simply a polynomial of degree $p_{max}$, but taking the $pth$ rate of change of the trajectory gives a dynamical definition, i.e. a state transition matrix.
The observation equation is trivial due to the fact that we observe directly the state that we want to estimate, i.e.:

$$X = X + \eta, \tag{3}$$

where $\eta$ is the noise of the measurement with unknown probability density function.

### 4.2. Observation and Error Windows

For the estimation of the future state and its update, we use all measurements contained within a sliding observation window of $n$ entries. Estimators that minimize the

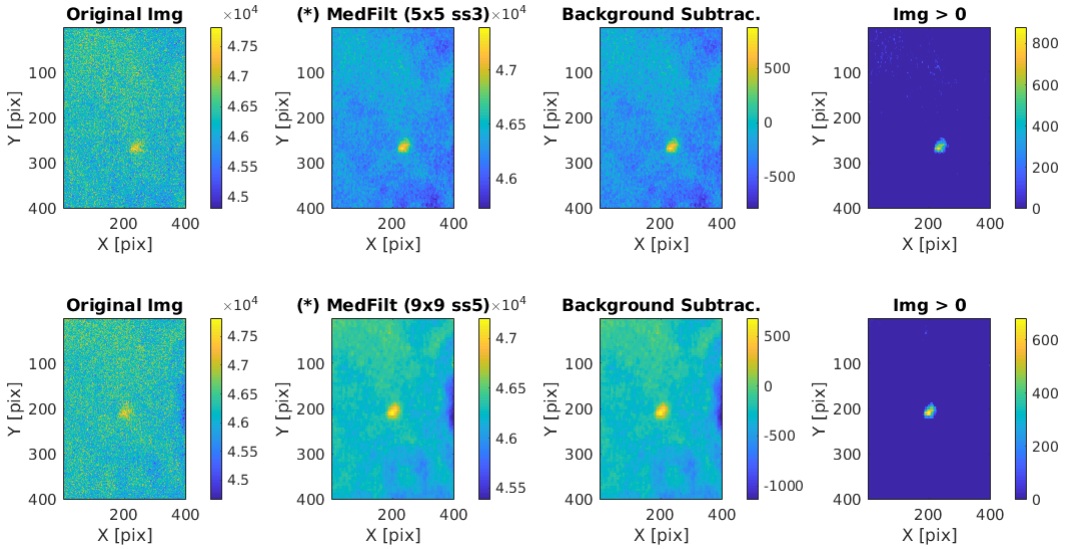


*Figure 3. Comparison of the resulting centroid after using a different set up for the pre-processing step, i.e. convolution between the raw subframed image and median kernel. The top sequence uses a median filter with a kernel of 5 pixels x 5 pixels with a step size of 3 pixels, while the bottom sequence uses a kernel of 9 pixels by 9 pixels with a step size of 5 pixels. Note that in the top sequence the object image is not centered in the subframe due to the impact of the non-filtered background pixels from the previous image. Unit colorbars: ADU.*

*mean square error* are arguably sensitive to outliers due to their low breakdown point. An example of an outlier coming from the object recognition phase can occur, e.g. due to a passing cloud. The estimated centroid will most likely correspond to the center of gravity of all the unmasked pixels which belong to the cloud not to the object of interest. In order to filter outliers, we use a sliding error window ($sew$) defined by the observed-minus-computed (OmC) state of the object image for the $n$ entries of the sliding observation window.

As soon as a new observation becomes available, we subtract it from its prediction, defining the term $OmC_t$, and compare it against $\tau = MED(sew) \pm kMAD(sew)$ computing it over all $n$ OmC entries in the sliding error window. Our null hypothesis is that $OmC_t$ is within the bounds $\pm\tau$. If the alternate hypothesis results true, then the observation acquired at epoch $t$ is marked and not accounted for within the sliding observation window.

Note that during the tracking a sudden change in the trajectory can happen. In that case, the next $n/2$ observations will be marked as outliers, however, the $n/2+1$ incoming observation will correct the estimated $\tau$, avoiding the saturation of the filter marking as good observations those within the newly estimated $\pm\tau$.

### 4.3. Results and Discussion

We present an interesting case for a LAGEOS-1 pass observed on April 20, 2019. The reason for selecting this target relies on its low signal-to-noise ratio, which evinces a perfect case for testing the precision, accuracy and reliability of the algorithm. For the accuracy, the solution extracted using the software AstroImageJ [2] will define our ground truth. In Figure 4 we show the component-wise solutions obtained using AstroimageJ (aij), the estimated state from the object recognition procedure (objrec), and the predicted state derived from the active tracking (track). In Figure 4 we are able to see:

1. **Initialization of the sliding observation window.** The algorithm stores the first 10 entries to initialize the $sow$. The solution provided by the object recognition procedure is in agreement with respect to the solution extracted using aij.

2. **Change in component X and outlier in Y.** We can see how the X component is treated at the beginning as an outlier neglecting all incoming measurements, but after the 5th new measurement, the filter becomes responsive again. In the Y component we can see two spurious measurements neglected by the active tracking.

3. **Exclusion of outlier.** We can see that an important outlier is neglected by the tracking solution, smoothing the trajectory of the object image as receiving new observations.

The maximum error between the solution provided by aij and ours is that of 20 pixels. Considering a pixel scale of 0.173 arcseconds/pixel, we conclude that the algorithm performs at the required level, i.e. can block the target within the field of view of the laser beam which is $\approx 20$ arcseconds.

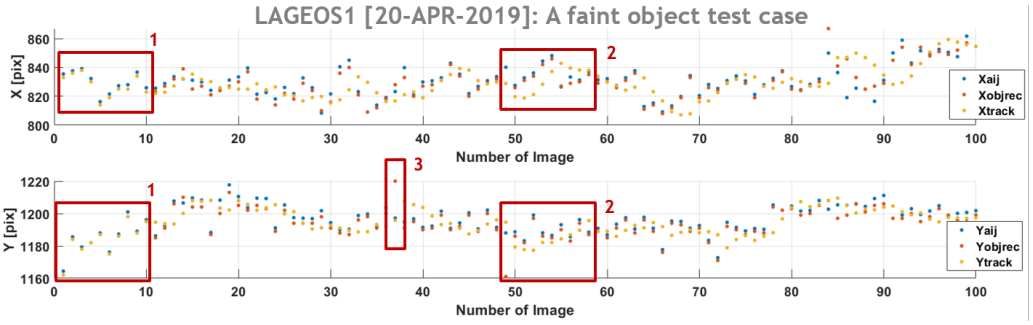


*Figure 4. Lageos-1 case study to validate the estimation of the centroid against the solution provided by AstroImageJ. We show the component-wise solutions obtained using AstroimageJ (aij), the estimated state from the object recognition procedure (objrec), and the predicted state derived from the active tracking (track).*

## 5. CASE STUDY: H-2A

In Subsection 3.5 we introduced a challenging pass due to the observation conditions: daylight, low elevation, passing clouds and short exposure time. In Figure 5 we show the observation geometry for the observed pass from the SwissOGS.

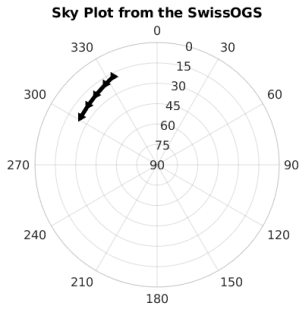


*Figure 5. Observation geometry for the rocket body H-2A observed from the SwissOGS on October 11, 2019, at 15:43 UTC.*

Furthermore, this case highlights the benefits from an active tracking approach instead of an initial orbit determination. By the time that observations will be collected for the initial orbit determination and newly ephemerides will be generated and integrated into the observing system, the target will most likely be lost. In Figure 6 we can see the different solutions for the retrieval of the object's image centroid using only the object recognition algorithm, using active tracking, and the solution extracted from aij. A striking feature is the remarkable drift starting at the 18th second. At that particular epoch, few clouds obscured the object preventing the estimation of its centroid until second 25. After ignoring the first outliers, the filter finally follows the object until new accurate observations become available. That particular event was not successfully overcome by the aij solution: the coordinates of the object's centroid for those frames covered by clouds were introduced manually for the sake of comparison. The other two discontinuities at seconds 54 and 104 are due to the interaction of the observer to re-center the target while storing images. The latter two events triggered a halting event in aij. In our case, we were able to process the complete pass without halts thanks chiefly to the width of the subframe, which mainly permitted the recognition of the object within a wider space search than the one used by aij. The right subplots in Figure 6 show that our centroid's detection are in agreement with the ones obtained from the aij solution. The tracking solution proves its smoothness after the relatively scattered observations of the object's centroid attributed mainly to the low intensity contrast between source and background, cloud presence, freezing of the seeing, etc.

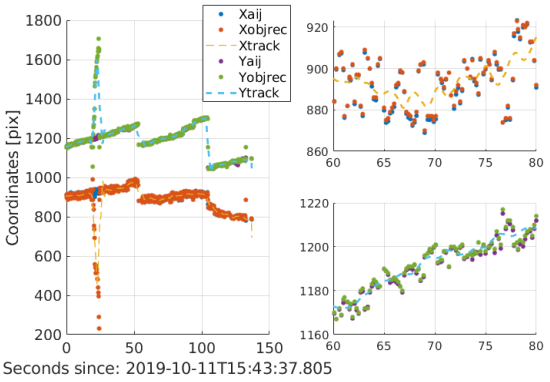


*Figure 6. Centroiding solutions for the H-2A pass on October 11, 2019. We show the component-wise solutions obtained using AstroimageJ (aij), the estimated state from the object recognition procedure (objrec), and the predicted state derived from the active tracking (track). The right plots depict a detailed portion of the pass for the x component (top) and y component (bottom).*

After the extraction of the centroid, the placement of source and background apertures in the original subframe permitted us to extract the apparent instrumental magnitudes, which are shown in Figure 7.

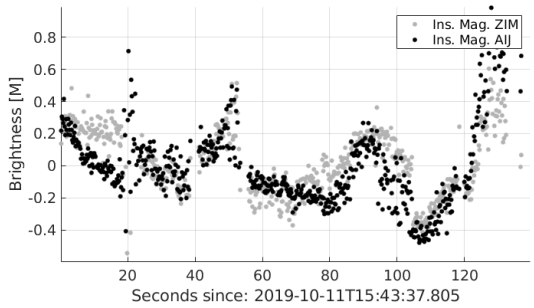


*Figure 7. Extracted instrumental magnitudes using our real-time solution (ZIM) and the post-processed solution using aij.*

In general our solution and the one provided by AstroImageJ show a significant dispersion due to the aforementioned eventualities. Nonetheless, we can notice certain periodicity that might correlate with the attitude and attitude motion of the target. Note that the represented light curve was detendred to remove the contribution of the slant range and phase angle. The observables collected during the observation of this pass are: azimuth, elevation and apparent brightness. Unfortunately, for this particular case we did not retrieve any laser ranges.

## 6. SUMMARY

The use of an active tracking approach might be critical to reduce drastically the uncertainty of the target's state within single passes. Moreover, after the successful tracking, the newly estimated state may be propagated and ephemerides can be sent to partner stations, which can reacquire the target and further improve the knowledge of the target's state.
The core algorithms for observation strategies such as the stare and chase are based on object recognition and tracking modules. To be successful in the aforementioned observation strategy, the derivation of robust, efficient and implementable algorithms becomes imperative. Through this work, we presented:

- **Centroid and apparent brightness estimation** through a sequence of image processing steps. Those steps are the cropping of the full raw image into a subframe, the convolution of the subframe image against a median kernel, the background subtraction, and finally the estimation of the centroid as the weighting average of all remaining positive pixels. Once the centroid is available we place source and background apertures and retrieve the apparent magnitude of the target.
- **Active tracking** based on the estimation of the target's state at a future epoch besides the update of its current state making use of its past n historical records. The inclusion of the sliding error window enhances the robustness of the otherwise sensitive M-estimator used for the estimation of the trajectory. We presented a validation of the algorithm by comparing our solution with the one extracted from the software AstroImageJ.
- **Presented a case study** for the rocket body H-2A, observed with very challenging conditions: daylight, low culmination, cloud presence all in real time. The results demonstrated an accurate procedure to correct for the pointing of the telescope beside the real-time collection of azimuth, elevation, apparent brightness and ranges. For the case study of H-2A, we did not collect ranges, but we have other cases that prove that capability.

## ACKNOWLEDGMENTS

The first author would like to thank the Swiss National Science Foundation for providing the funds for the current study through grant 200020-175795. Likewise, he would like to thank Dr. Emiliano Cordelli for all fruitful discussions and insights, which improved the presented work.

## REFERENCES

1. *Space-track. two line elements*. https://www.space-track.org/auth/login. Accessed: 2020-10-05.
2. K. A. COLLINS, J. F. KIELKOPF, K. G. STASSUN, AND F. V. HESSMAN, *Astroimagej: Image Processing and Photometric Extraction for Ultra-Precise Astronomical Light Curves*, The Astronomical Journal, 153 (2017), p. 77.
3. E. CORDELLI, J. RODRIGUEZ-VILLAMIZAR, P. SCHLATTER, AND P. LAUBER, *Real time improvement of orbits of space debris by fusing SLR and astrometric data acquired by a night-tracking camera*, in 21st International Workshop on Laser Ranging, 2018.
4. ESA SPACE DEBRIS OFFICE, *ESA's Annual Space Environment Report*, 2020. Revision 4.0.
5. S. B. HOWELL, *Handbook of CCD astronomy*, vol. 5, Cambridge University Press, 2006.
6. INTER-AGENCY SPACE DEBRIS COORDINATION COMMITTEE, *Space Debris Mitigation Guidelines, IADC-02-01*, 2020. Revision 2.
7. M. R. PEARLMAN, J. J. DEGNAN, AND J. M. BOSWORTH, *The International Laser Ranging Service*, Advances in Space Research, (2002).
8. J. RODRIGUEZ-VILLAMIZAR, E. CORDELLI, AND T. SCHILDKNECHT, *The new stare & chase procedure at the swiss optical ground station and geodynamics observatory zimmerwald*, in Proc. 1st NEO and Debris Detection Conference, Darmstadt, Germany, 22-24 January 2019.

9. P. J. ROUSSEEUW AND C. CROUX, *Alternatives to the median absolute deviation*, Journal of the American Statistical Association, (1993).
10. D. WILLIAMS ET AL., *Weighing the odds: a course in probability and statistics*, Cambridge University Press, 2001.